Optics Letters

Image registration for daylight adaptive optics

MICHAEL HART

College of Optical Sciences, University of Arizona, Tucson, Arizona 85721, USA (mhart@optics.arizona.edu)

Received 15 January 2018; revised 18 February 2018; accepted 19 February 2018; posted 20 February 2018 (Doc. ID 318891); published 14 March 2018

Daytime use of adaptive optics (AO) at large telescopes is hampered by shot noise from the bright sky background. Wave-front sensing may use a sodium laser guide star observed through a magneto-optical filter to suppress the background, but the laser beacon is not sensitive to overall image motion. To estimate that, laser-guided AO systems generally rely on light from the object itself, collected through the full aperture of the telescope. Daylight sets a lower limit to the brightness of an object that may be tracked at rates sufficient to overcome the image jitter. Below that limit, wave-front correction on the basis of the laser alone will yield an image that is approximately diffraction limited but that moves randomly. I describe an iterative registration algorithm that recovers high-resolution long-exposure images in this regime from a rapid series of short exposures with very low signal-to-noise ratio. The technique takes advantage of the fact that in the photon noise limit there is negligible penalty in taking short exposures, and also that once the images are recorded, it is not necessary, as in the case of an AO tracker loop, to estimate the image motion correctly and quickly on every cycle. The algorithm is likely to find application in space situational awareness, where high-resolution daytime imaging of artificial satellites is important.

OCIS codes: (010.1080) Active or adaptive optics; (010.1330) Atmospheric turbulence; (010.7350) Wave-front sensing.

https://doi.org/10.1364/OL.43.001391

High-resolution imaging through the Earth's atmosphere requires that the blurring effects of turbulence-induced wave-front aberration be corrected either with adaptive optics (AO) or by numerical image restoration. The former is preferred where possible because of the improved sensitivity arising from a more advantageous distribution of photon noise in the light from the object itself. While AO systems on large telescopes are presently used exclusively at night, a number of applications would benefit from the use of AO during the day. That is challenging for a number of reasons. Seeing in the daytime is typically worse than at night because of thermal plumes arising from solar heating of the ground. The wave-front sensor (WFS) suffers from shot noise in the bright sky background and may also simply saturate, preventing it from providing any useful information.

Beckers and Cacciani [1] suggested in 2001 that the value of extremely large telescopes (ELT) of 25 m and bigger could be extended by using them with laser-guided AO at thermal infrared wavelengths during the day since the limitation imposed by the sky background in these bands is no worse than at night. High-resolution daytime imaging of artificial satellites would also be of value to the space community [2]. Observations of low-Earth orbit satellites are now largely restricted to so-called terminator mode around dawn and dusk when the satellite is sunlit, but the sky is still dark. It is presently also very challenging to observe an important class of objects in sun-synchronous orbits that always appear over a given site at the same time of day.

In that same paper, Beckers and Cacciani suggested that a practical daytime AO system could be implemented with a sodium laser guide star (LGS) when the WFS employs a magneto-optical filter (MOF) [3–5]. An MOF offers a transmission profile of typically just 10 pm width [6], which passes the LGS light with high efficiency but blocks light at all other wavelengths, very effectively reducing the sky background. We have shown experimentally that the combination of a sodium LGS and MOF is viable for daytime AO wave-front sensing [7].

It is well known that global wave-front tilt cannot be estimated from LGS signals because of the unknown beam wander on the upward path. Generally, an independent tracking camera is used, looking at light from the object of interest itself or, in astronomical usage, a nearby reference star. But what if no suitable object is available? High-order wave-front corrections applied by reference to the LGS with no tip-tilt correction will result in an image that is instantaneously close to diffraction limited, but that moves around in the focal plane on the scale of the atmospheric coherence time τ_0 [8]. At very large telescopes the effect of a finite outer scale of turbulence may admit modest correction even without a tip-tilt star [9]. However, on telescopes with diameters of a few meters or less, a single exposure substantially longer than τ_0 will be blurred almost as badly as if no AO correction had been applied at all. Yet, as the object becomes fainter, the only way to maintain a given signal-to-noise ratio (SNR) in the presence of high background illumination is to accumulate signal over longer periods. This is a fundamental physical limitation.

Imaging at visible wavelengths during the day is an extreme background-limited case where many objects of interest will be too faint to be tracked with sufficient speed and accuracy to correct image motion in real time. On the other hand, in this regime even short exposures that freeze the motion will be dominated by background shot noise rather than read noise from

the detector. With negligible noise penalty, then, a scheme can be considered whereby a long-exposure image is synthesized from a sequence of short exposures with the motion of the object computed by an image registration algorithm and applied as the image shifts in the computer. This shift-and-add method [10] is already a well-known paradigm in astronomy. Robo-AO is an example of a laser-guided AO system that successfully exploits it, using a standard cross-correlation between each frame and a theoretical point-spread function [11]. Many other algorithms have been developed for image registration, based, for example, on maximum likelihood estimation [12,13] under the assumption of various noise models. In this Letter, I propose an algorithm that demonstrates robustness under conditions of very low SNR.

There are two key differences between real-time motion correction and numerical image registration that allow the latter to succeed where the former may fail. Both past and future history are available to the registration algorithm, and it is not critical to get the answer right on the first attempt. An iterative approach, possibly time-consuming, may in principle work. The method described here exploits both these ideas under the assumption that the object appears the same in all frames.

The distinguishing characteristic of a good co-added image stack, where the image shifts are well estimated, compared to a bad one is the power in angular frequencies between the seeing limit $f_{\mathrm{SL}} = r_0/\lambda$ and the diffraction limit $f_{\mathrm{DL}} = D/\lambda$, where r_0 is the atmospheric coherence length, D is the telescope diameter, and λ is the mean wavelength of observation. Outside this range, angular frequencies are not diagnostic of the image shifts. The uncorrected image motion does not degrade frequencies below f_{SL}, and those higher than f_{DL} are attributable solely to noise. The search algorithm seeks image shifts that maximize the power spectrum of the co-added image within this range.

The algorithm carries out an iterative constrained Monte Carlo search for optimal values of the image shifts. The steps for a single iteration are summarized in Fig. 1. To begin, the image sequence is binned in time by a factor B to improve the SNR. Then an outer radius f_{UL} for the optimization region in the Fourier plane is computed. This depends on the binning: essentially, the larger the value of B, the worse the blurring in the binned (and as-yet-unshifted) images. The radius for enhancement of the power spectrum is therefore not expected to extend all the way to the diffraction limit. To compute an appropriate value for f_{UL}, we start from the structure function, which quantifies the variance of the change in tilt over a time interval Δt. For short time intervals $\Delta t < D/V$, less than the beam crossing time for turbulence driven by wind at speed V, the structure function is reasonably approximated by [14]

$$S^2(\Delta t) = 1.32(\lambda/D)^2(D/r_0)^{-1/3}(\Delta t/\tau_0)^2. \quad (1)$$

The uncorrected tilt blurs the binned images with a Gaussian kernel of angular width corresponding to this variance with $\Delta t = Bt_{\mathrm{exp}}$, where t_{exp} is the cadence of the original image sequence. For observations at visible wavelengths with telescopes of $D > 1$ m, we will typically find ourselves in the regime where $Bt_{\mathrm{exp}} < D/V$, so the assumption of short time scales will be justified. The high-frequency cutoff f_{UL} is taken to be the half width at half-maximum of the Fourier transform of the blur function, also a Gaussian, subject to the constraint $f_{\mathrm{UL}} \le f_{\mathrm{DL}}$.

$$f_{\mathrm{UL}} = 0.42/S(Bt_{\mathrm{exp}}). \quad (2)$$

The algorithm then computes a metric ε, defined as the sum of the power spectrum of the co-added image stack over an annulus between f_{SL} and f_{UL}. A Monte Carlo search over image shifts ξ_k, υ_k maximizes ε according to

$$\underset{\xi_k,\upsilon_k}{\operatorname{argmax}}\,\varepsilon = \sum_{u^2+v^2>f_{\mathrm{SL}}^2}^{u^2+v^2<f_{\mathrm{UL}}^2} \left| F\left(\sum\nolimits_k I_k(x+\xi_k, y+\upsilon_k)\right)_{u,v} \right|^2. \quad (3)$$

In Eq. (3), $F()$ represents the Fourier transform, I_k is the kth image in the binned sequence, and (u, v) and (x, y) are coordinates in the Fourier plane and image plane, respectively.

The shifts are expanded by the binning factor B using sinc interpolation to cover the full sequence, and the images are recentered accordingly. Finally, the process is repeated with B reduced by a factor of 2, rounded up to the nearest integer. Iterations continue until either there is no further significant change in ε or $B = 1$.

The interpolation relies for its effectiveness on the general shape of the temporal structure function of the image motion. On short time scales, the expectation value S varies approximately linearly with time delay, with the obvious implication that motions over short time delays will be less than those over longer delays. Interpolation from longer time scales will therefore tend to yield improvement on shorter time scales. This behavior of S also implies a requirement that t_{exp} be comparable to τ_0; short exposures acquired with low duty cycle will not be well corrected with this technique. Furthermore, setting the summation limits in Eq. (3) requires explicit estimates of r_0 and τ_0. The use of imprecise values, however, will affect the algorithm's efficiency rather than its accuracy, so typical values for a site may be used, and those are generally known.

The method has been tested with simulated data constructed from a real sequence of observations of the Hubble Space Telescope (HST) made with the AO system at the 3.6 m Advanced Electro-Optical System (AEOS) telescope on Mt. Haleakala, Hawaii [15]. The sequence comprised 250 contiguous 512 × 512 frames with 2 ms exposure recorded through an optical filter centered at approximately 800 nm. The images are close to diffraction limited; an example is shown on the right of Fig. 2.

To make the simulated data, the recorded sequence was replicated 10 times to form a sequence 2500 frames long. Image motion was modeled by shifting each frame, using the Fourier shift theorem, according to two sequences of pseudo-random values obeying Kolmogorov statistics for wave-front tilt. The values, plotted in Fig. 3, were scaled to a standard deviation of 0.25 arcsec, the expected value for $r_0 = 10$ cm at 500 nm

1. Bin frames by factor B in time.
2. Set Fourier mask diameter.
3. For each binned image k, compute a large number of random trials of ξ_k, υ_k; select values that maximize ε.
4. Interpolate shifts over full unbinned data sequence using sinc interpolation.
5. Recenter all images using interpolated shifts.
6. If final value of ε is within 3% of previous iteration, or $B = 1$, terminate.
7. Set $B = B/2$ and return to Step 1.

Fig. 1. Steps in the search algorithm.

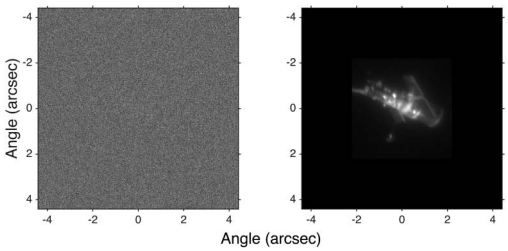

Fig. 2. One of the AO-corrected images from the sequence collected at the AEOS telescope and used in this study. (Left): with simulated added noise; (right): the original image shown on a square-root scale. Video available as Visualization 1.

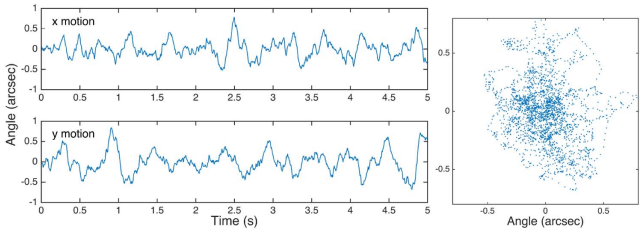

Fig. 3. Random motion assigned to the 2500 data frames, modeling 5 s of elapsed time at 2 ms per frame, shown as linear plots (left) and a scatter plot (right).

[16]. Each frame was then replaced with the average of itself and the next frame in the sequence. This procedure crudely models the residual motion blur to be expected when the object is not actively tracked by an AO system. The mean images with and without the artificial shifts are shown in Fig. 4. Figure 5 illustrates the difference in spatial frequency content quantified in Eq. (3). Finally, photon noise was added, assuming an integrated I-band object brightness of $m_{\mathrm{obj}} = 9$, and sky background surface brightness of $m_{\mathrm{sky}} = 4$ arcsec^{-2} [17,18]. For completeness, Gaussian detector read noise of 3 electrons rms was also added, although the contribution is negligible in comparison to the shot noise: the mean sky background per pixel was 304 photons. The model parameters are summarized in Table 1.

The left panel of Fig. 2 shows one of the modeled data frames: the object has all but disappeared. The mean object flux per frame is 10,300 photons, leading to an SNR per illuminated pixel of less than 0.03. For the entire object, the SNR is about 4.

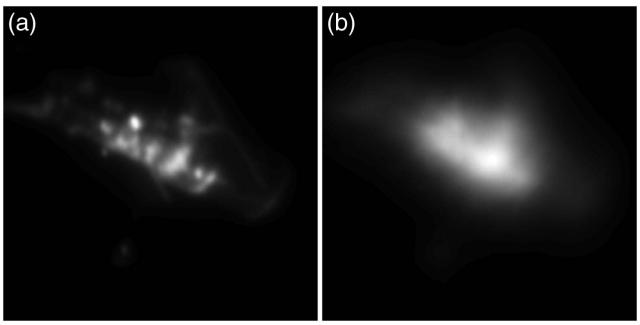

Fig. 4. Averages of the 2500 frame sequences before the addition of noise. (a) Unshifted frames. (b) Shifted frames. Both images on linear gray scale.

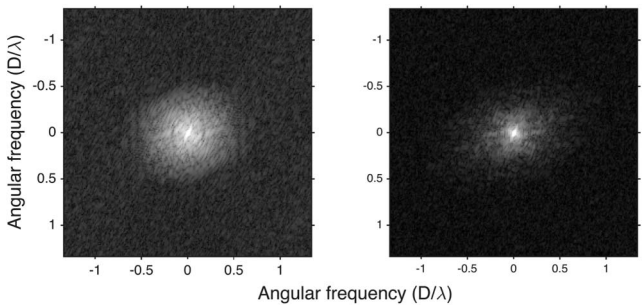

Fig. 5. Square root of the power spectrum of the noise-free HST images. (Left): original AO-corrected frames. (Right): with artificial shifts. Both images on the same logarithmic scale.

The results of applying the search algorithm to the HST data are shown in Fig. 6. The algorithm converged in three iterations. The result is encouraging: compared to the true positions in Fig. 3, the residual is 0.037 arcsec or 0.81 λ/D. The final image has a resolution close to the diffraction limit.

In the case simulated here the object is too faint for effective real-time tip-tilt correction. Given the SNR for detection, we should expect that the accuracy of tip-tilt estimation from a single frame would be one quarter of the object's extent, or about 1.0 × 0.4 arcsec along and across the body of the HST. That is already coarser than the entire atmospheric tilt error of 0.25 arcsec rms. Attempting to integrate past data would not help; to achieve the SNR needed to match the residual tilt error of 0.037 arcsec found by post-processing would require a look-back of over 500 frames, or more than 1 s. That is long enough that the atmospheric tilt will explore its full range, preventing any precise measurement.

Three parameters of the algorithm are set heuristically, though automatically. The initial value of the binning B is determined from Eq. (1) by setting S^2 equal to half its asymptotic value for large Δt, given by $S^2_{\mathrm{max}} = 2\sigma^2_{\mathrm{tilt}} = 1.20(\lambda/D)^2(D/r_0)^{5/3}$ [19]. (This is twice the variance of the two-axis motion.) In this way, the SNR is improved, but the images are not blurred all the way to the seeing limit: there is leverage to find the low-frequency motion. The search radius for the shift values in Step 3 (Fig. 1) is set to 5× the expected motion in time interval Bt_{exp}, or $5S(Bt_{\mathrm{exp}})$. Finally, the number of random trials is set to 100, which puts the mean spacing between the trial shifts at $0.8S(Bt_{\mathrm{exp}})$.

The algorithm is not real time. On a 2016 MacBook Pro, it takes about 10 min to find the optimal shifts for the 2500 frame HST simulation, with about two thirds of that time spent finding the shifts and one third actually recentering the images.

Table 1. Parameters of the Simulated Data

Parameter	Value
Telescope diameter	3.6 m
Overall optical efficiency	25%
Center wavelength	800 nm
Optical bandwidth	22%
Atmospheric coherence length r_0	10 cm at 500 nm
Atmospheric coherence time τ_0	1 ms at 500 nm
Filter magnitude zero point	8.0×10^9 photon m^{-2} s^{-1}
Object brightness	$m_{\mathrm{obj}} = 9$
Sky brightness	$m_{\mathrm{sky}} = 4$ arcsec^{-2}
Detector read noise	$3e^-$ rms
Integration time	2 ms
Pixel scale	0.0172 arcsec

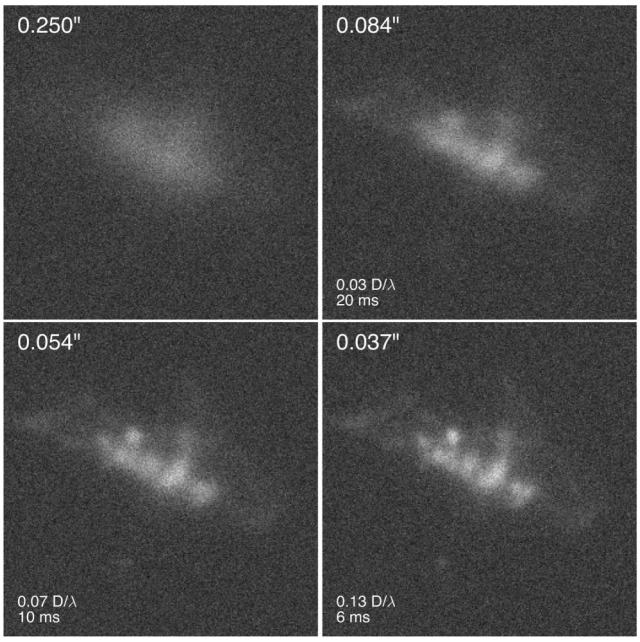

Fig. 6. Results of the image shift computations as they improve over three iterations. At top left is the mean image before any correction. The number at the top of each frame quantifies the rms residual single-axis position error. At the bottom are the Fourier search radius and the temporal binning factor. The lower right panel shows the result at convergence.

A thorough analysis of the performance of the algorithm would account for the spectrum of the object since that has a direct effect on the sensitivity of ε to changes in the image shifts. It is unlikely that the object spectrum will be known in advance, but one may still estimate from general considerations the minimum surface brightness where the method will have some value. To have any traction, the initial binning must yield an equivalent integration time shorter than the time for the structure function S^2 to saturate. For delays $\Delta t > D/V$, where the aperture no longer acts as a filter, S^2 follows a different form than Eq. (1) and becomes $S^2(\Delta t) \approx 1.11(\lambda/D)^2(\Delta t/\tau_0)^{5/3}$. The maximum integration time $t_{\max}$ can be estimated by setting $S^2(t_{\max}) = 2\sigma_{\text{tilt}}^2$, or $t_{\max} = 1.05\tau_0(D/r_0)$. For the HST simulation, this is 38 ms.

For significant improvement, the integration time must be sufficient for features on spatial scales about a factor of two smaller than the seeing limit to be observable at SNR > 1. Insisting that the object signal from a patch of angular diameter $\lambda/2r_0$ exceed the sky noise from the same patch leads to the requirement $F_{\text{obj}} > 4/(\pi D)(F_{\text{sky}}/t_{\max})^{1/2}(\lambda/2r_0)^{-1}$, where F_{obj} and F_{sky} are, respectively, the object and sky fluxes in photon $\text{s}^{-1}\,\text{m}^{-2}\,\text{rad}^{-2}$ received at the detector. Substituting for $t_{\max}$ yields

$$F_{\text{obj}} \gtrsim (F_{\text{sky}}/\tau_0)^{1/2}(r_0/D^3)^{1/2}(2r_0/\lambda), \quad (4)$$

where in the spirit of the approximation I neglect factors of order unity, and the terms highlight, respectively, the temporal, spatial, and angular dependencies. As one would expect, larger diameter telescopes have a clear advantage.

The HST simulation modeled a source of solid angle 4.8 arcsec^2 and a mean surface brightness of 10.7 mag arcsec^{-2}, yielding 10,300 photons per frame. Equation (4) suggests that in this case some correction might be obtained on objects as faint as 2200 photons per frame, about 1.7 mag arcsec^{-2} fainter.

In astronomical terms, an object with surface brightness $m_I \sim 12$ arcsec^{-2} is not faint. Even on an 8 m telescope observing in the K band where the daytime sky is about magnitude 6 arcsec^{-2} [20], the limiting surface brightness is about 13.6. Only with the advent of the ELTs will it be possible to approach potentially interesting surface brightnesses of 16 or 17 arcsec^{-2} in the visible and near IR bands during the day. It is worth noting that a tip-tilt natural guide star of the same brightness within the isokinetic angle of an object of interest would indeed allow access to even fainter sources, although the integration times required to overcome the high background are likely to be prohibitive in all cases but the most urgent targets of opportunity.

On the other hand, artificial satellites in low- and mid-Earth orbits seen in reflected sunlight will be accessible with this method. Since satellites move at non-sidereal rates, it is not feasible to use natural stars as tip-tilt reference beacons; light from the object itself must be used. Satellite brightnesses depend strongly on the nature of the reflecting surface and the wavelength. On average, though, and regardless of their distance, satellites appear about as bright per unit solid angle as the moon, or about magnitude 3 arcsec^{-2}. Solar-illuminated objects that are resolved by large telescopes dedicated to space situational awareness will therefore generally be observable. Future work will compare the algorithm described here to other candidate image registration methods such as cross-correlation.

Acknowledgment. The author thanks J. Codona for valuable discussions and critical readings of the Letter.

REFERENCES

1. J. M. Beckers and A. Cacciani, Exp. Astron. **11**, 133 (2001).
2. M. C. Roggemann, D. Douglas, E. Therkildsen, D. Archambault, R. Maeda, D. Schultz, and B. Wheeler, in *Proceedings of the Advanced Maui Optical and Space Surveillance Technologies Conference*, S. Ryan, ed. (2010).
3. A. Cacciani and A. M. Fofi, Sol. Phys. **59**, 179 (1978).
4. C. Y. She, J. R. Yu, H. Latifi, and R. E. Bills, Appl. Opt. **31**, 2095 (1992).
5. H. Chen, M. White, D. A. Krueger, and C. Y. She, Proc. SPIE **2833**, 46 (1996).
6. W. Kiefer, R. Löw, W. Jörg, and I. Gerhardt, Sci. Rep. **4**, 6552 (2014).
7. M. Hart, S. M. Jefferies, and N. Murphy, J. Astron. Telesc. Instrum. Syst. **2**, 040501 (2016).
8. F. Rigaut and E. Gendron, Astron. Astrophys. **261**, 677 (1992).
9. R. Davies, S. Rabien, C. Lidman, M. Le Louarn, M. Kasper, N. M. Förster Schreiber, V. Roccatagliata, N. Ageorges, P. Amico, C. Dumas, and F. Mannucci, Telescope Instrum. **131**, 7 (2008).
10. R. H. T. Bates and F. W. Cady, Opt. Commun. **32**, 365 (1980).
11. C. Baranec, R. Riddle, N. M. Law, A. N. Ramaprakash, S. Tendulkar, K. Hogstrom, K. Bui, M. Burse, P. Chordia, H. Das, R. Dekany, S. Kulkarni, and S. Punnadi, Astrophys. J. **790**, L8 (2014).
12. D. Gratadour, L. M. Mugnier, and D. Rouan, Astron. Astrophys. **443**, 357 (2005).
13. M. Guillaume, P. Melon, P. Réfrégier, and A. Llebaria, J. Opt. Soc. Am. A **15**, 2841 (1998).
14. A. Kellerer and A. Tokovinin, Astron. Astrophys. **461**, 775 (2007).
15. L. C. Roberts and C. R. Neyman, Publ. Astron. Soc. Pac. **114**, 1260 (2002).
16. H. M. Martin, Publ. Astron. Soc. Pac. **99**, 1360 (1987).
17. H. Lin and M. J. Penn, Publ. Astron. Soc. Pac. **116**, 652 (2004).
18. B. LaBonte, Sol. Phys. **217**, 367 (2003).
19. R. J. Noll, J. Opt. Soc. Am. **66**, 207 (1976).
20. K. T. C. Jim, B. N. Gibson, and E. A. Pier, in *Proceedings of the Advanced Maui Optical and Space Surveillance Technologies Conference*, S. Ryan, ed. (2012).